Thermal Signal Spatial Quasi-Static Reconstruction: A Novel Feature Enhancement Algorithm for Microcrack Detection in Thermography

Junyan Liu [a,b,], Rongcheng Li [a,b], Fei Wang [a,b,*], Feng Yang [a,b], Stefano Sfarra [c], Zhuoyan Yue [a,b]*

[a] *School of Mechatronics Engineering, Harbin Institute of Technology, Harbin, 150001, P. R. China.*
[b] *State Key Laboratory of Robotics and System (HIT), Harbin, 150001, P. R. China.*
[c] *Department of Industrial and Information Engineering and Economics, University of L'Aquila 67100, Italy.*

**Address all correspondence to：Fei Wang and Junyan Liu, School of Mechatronics Engineering, Harbin Institute of Technology, Nangang District Xidazhi Street 92#, 150001, Harbin, Heilongjiang province, P. R. China. E-mail: Fei Wang (wangfeipublic@hit.edu.cn) and Junyan Liu (ljywlj@hit.edu.cn).*

Abstract

Active infrared thermography has been demonstrated to offer a wide range of applications in the domain of non-destructive testing, thanks to its multiple advantages. However, when applied to the detection and identification of minute defects on the surfaces of metals and other highly thermally conductive materials, the performance of conventional active infrared thermography is suboptimal. In this paper, a quasi-static reconstruction method based on spatial domain feature reconstruction is proposed to solve this problem. Combined with miniaturized detection equipment, this method enables reliable detection of cracks as narrow as 2 μm on titanium alloy surfaces, offering a novel approach for detecting microcracks on alloy surfaces. Based on the three-dimensional simulation model, the thermal response characteristics caused by crack defect are analyzed to provide theoretical support for the quasi-static reconstruction method proposed for different scanning methods. To verify the reliability of this method, a TC4 specimen containing cracks of various widths is prepared and a mobile laser scanning infrared thermography system is established, which demonstrates the potential for miniaturization and integration, broadening its applicability in industrial in-situ inspection endoscopic inspection.. Comparative experiments demonstrate that an appropriate combination of scanning method and reconstruction method can effectively suppress background signal interference caused by surface reflections, allowing for the reliable detection and identification of cracks with widths down to 2μm. Analysis indicates that the signal-to-noise ratio(SNR) is positively correlated with crack width, and feature extraction algorithms demonstrate a significant contribution to the improvement of SNR for cracks with a width of 2μm.

Keywords: Laser scanning infrared thermography, quasi-static reconstruction method, feature extraction algorithms, crack inspection, surface microcracks.

1. INTRODUCTION

With the development of industrial technology, new materials such as titanium alloys and superalloys are increasingly utilized in aerospace, chemical, marine, and shipbuilding due to their excellent fatigue resistance and corrosion resistance[1,2]. Among various factors affecting the safety of workpieces, fatigue-induced surface cracks represent a significant threat to equipment reliability[3-5]. These cracks typically originate at the microscopic level, forming imperceptible microcracks on material surfaces. Subsequently, they undergo rapid propagation, leading to material or structural fracture and failure, which causes the malfunction of the entire system[6,7]. Due to the location and the size of the crack, such defects are difficult to detect. Therefore, it is necessary to achieve crack detection accurately and efficiently. Furthermore, considering the complexity of the workpiece structures and operational environments, as well as preventing further damage to the workpiece, nondestructive testing technology plays an important role in surface crack detection and identification.

Traditional non-destructive testing methods face certain limitations. For instance, ultrasonic testing struggles to detect small defects near the surface of materials[8,9]. Radiographic testing, magnetic particle testing and penetrant testing are very effective for detecting surface cracks, but the equipment and procedures are complex and difficult to achieve automatic and in-situ detection[10-14]. Eddy current testing is sensitive to the roughness of material surfaces but suffers from relatively slow inspection speeds[15]. Infrared testing, as an emerging non-destructive testing technology, is widely used for qualitative and quantitative detection of internal defects such as delamination and debonding in composite materials owing to its non-contact nature, efficient, high detection accuracy, and visually interpretable results[16-18]. Particularly for challenging detection scenarios, such as shallow cracks on metal materials, the potential of active infrared thermography is gaining growing interest [19-21].

The presence of defects in metallic materials leads to localized variations in thermal conductivity. Therefore, when a heat flux is actively injected onto the specimen surface via a laser or halogen lamps, the heat conduction on the material surface will be locally effected, resulting in heat accumulation at the defect site and abnormal temperature rise. An infrared thermal imager is set to capture the abnormal temperature distribution on the material surface, thereby achieving crack identification.

In general, active infrared thermography employs a scanning motion technique to achieve large-area detection in a single instance. This approach typically results in a inspection outcomes manifesting as a long period of infrared video in which the heated area moves across the filed of view, complicating the discernment of defect results. At the same time, the detection of microcracks depends critically on the resolution capability of the infrared thermal imager, which usually requires high-performance specifications. Additionally, the difficulty of detection is further compounded when the cracks occur on materials with high thermal conductivity, particularly on highly reflective surfaces such as smooth surfaces. Consequently, an active infrared thermography method based on quasi-static reconstruction is proposed, with the aim of addressing these limitations to a certain extent. This method has the capacity to convert the spatial and temporal variation of thermal wave signals under the action of a mobile heat source into the temporal variation under the action of a static surface pulse heat source[22]. The data results after quasi-static reconstruction can be obtained through the implementation of feature extraction algorithms, including Fourier Transform (FT), Principal Component Transform (PCT), and Partial Least Squares Transform (PLST), to extract defect information, or through visual observation directly.[23].

The remainder of this article is organized as follows: Firstly, a three-dimensional model of a titanium alloy surface subjected to a mobile linear heat source is established, and the thermal response characteristics of surface crack defects are analyzed. Supported by the simulation results, the quasi-static reconstruction methods are proposed corresponding to different scanning methods. Secondly, a mobile laser scanning infrared thermography system is established, TC4 specimens with crack widths ranging from 2μm to 100μm are prepared for experimental validation. Then, the detection results are analyzed and compared, with defects quantitatively analyzed using the signal-to-noise ratio (SNR). Finally, the article is summarized.

2. THEORY AND METHODOLOGY

A. Thermal Wave Diffusion Model

The three-dimensional model of the titanium alloy surface subjected to a moving linear heat source is shown in Fig.1. Assuming that the energy density of the linear laser follows a Gaussian distribution, when a linear laser is acted on the surface of the material, the irradiated area absorbs heat and diffuses into the interior of the material. As the linear laser scanning motion progresses, different positions are illuminated. Therefore, the heat source of the material can be represented as follows:

$$
\begin{cases}
q(x,y,0,t) = Q \times \exp\left(-2\dfrac{\left(x - x_0(t)\right)^2}{r_0^2}\right) \\
x_0(t) = -\dfrac{L}{2} + vt
\end{cases}
\tag{1.1}
$$

where $q(t)$ is the heat source, Q is the power density of laser, taken as 40000W/m^2, $x_0(t)$ and r_0 are the center coordinate and the half width of the linear laser spot, respectively. L represents the length of the simulation area, and v donates the movement speed of the linear laser spot.

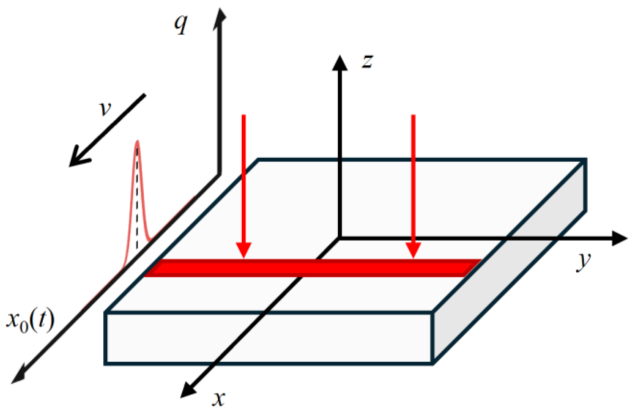

Fig.1 Three-dimensional model of the titanium alloy surface

The three-dimensional heat conduction equation can be written as:

$$
k_x \frac{\partial^2 T(x,y,z,t)}{\partial x^2} + k_y \frac{\partial^2 T(x,y,z,t)}{\partial y^2} + k_z \frac{\partial^2 T(x,y,z,t)}{\partial z^2} + q(t) = \rho c_p \frac{\partial T(x,y,z,t)}{\partial t} \tag{1.2}
$$

where k represents the thermal conductivity of the material, T is temperature, ρ stands for the density, and c_p is the specific heat capacity. Considering the ambient temperature as T_{am}, the initial temperature condition can be written as:

$$
T(x,y,z,t)\big|_{t=0} = T_{am} \tag{1.3}
$$

Considering the radiative and convective heat transfer on the material surface, the boundary conditions of the equation can be expressed as follows:

$$
-k_z \frac{\partial T(x,y,z,t)}{\partial z}\bigg|_{z=0} = q(x,y,0,t) + h_f\left[T_{am} - T(x,y,0,t)\right] + \varepsilon\sigma\left[T_{am}^4 - T(x,y,0,t)^4\right] \tag{1.4}
$$

$$
-k_z \frac{\partial T(x,y,z,t)}{\partial z}\bigg|_{z=-H} = h_r\left[T_{am} - T(x,y,-H,t)\right] + \varepsilon\sigma\left[T_{am}^4 - T(x,y,-H,t)^4\right] \tag{1.5}
$$

$$
-k_x \frac{\partial T(x,y,z,t)}{\partial x}\bigg|_{x=L/2} = -k_x \frac{\partial T(x,y,z,t)}{\partial x}\bigg|_{x=-L/2} = 0 \tag{1.6}
$$

$$-k_y \frac{\partial T(x,y,z,t)}{\partial y}\bigg|_{y=W/2} = -k_y \frac{\partial T(x,y,z,t)}{\partial y}\bigg|_{y=-W/2} = 0 \tag{1.7}$$

where h_f and h_r are the convective heat transfer coefficients for the front surfaces and the rear surfaces, respectively. H and W are the thickness and width of the simulation area, respectively. $q(x,y,0,t)$ represents the heat source distribution of laser excitation. ε denotes the surface emissivity of the material, and σ is the Stefan-Boltzmann constant.

The model is solved using COMSOL Multiphysics 6.1. The simulation domain and its meshing is shown in Fig.2. Three cracks are set with a width and depth of 20μm and a length of 10mm, oriented at 0°, 90°, and 45° relative to the scanning direction, respectively. The length of the simulation area is taken as 40mm, and the scanning speed is 8mm/s.

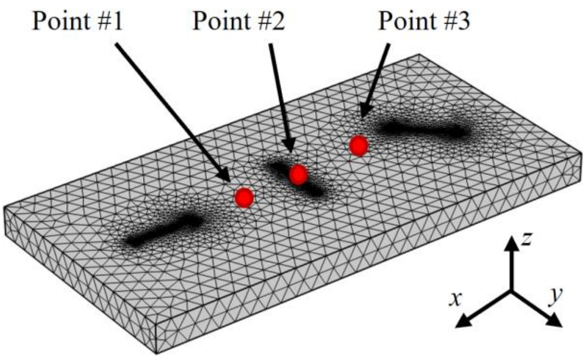

Fig.2 Grid division of simulation model

Fig.3 shows the temperature evolution around three crack defects. When the heat flux interacts with the surface, the presence of defects causes localized temperature elevation compared to the surrounding sound material. As the heat flux approaches the defect, this temperature contrast become increasingly apparent. The angle between defects and scanning direction also has an impact on temperature changes. When the angle is 0°, the temperature difference is minimal. Conversely, at angles of 45° or 90°, the temperature difference is substantial.

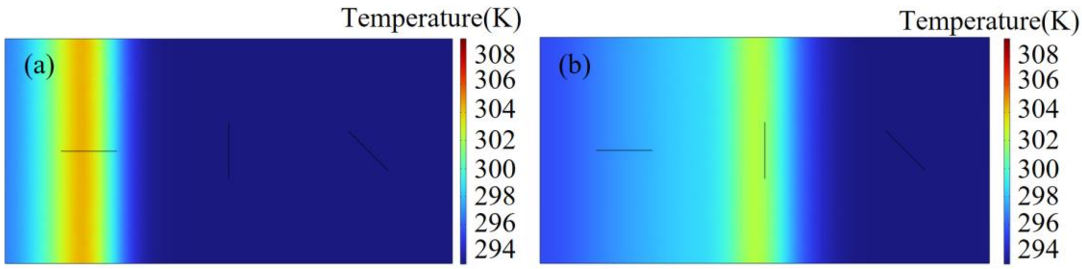

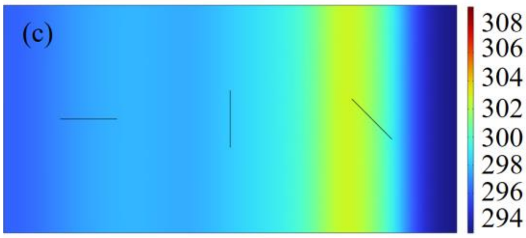

Fig.3 Temperature changes around crack defects at angles of (a) 0°, (b)90° and (c)45°

As shown in Fig.2, three points are selected around the crack defect along the scanning direction, with the Point #1 and Point #3 taken at the non-defect area and the Point #2 taken at the center of the defect area. The temperature variation over time at different points is shown in Fig.4.

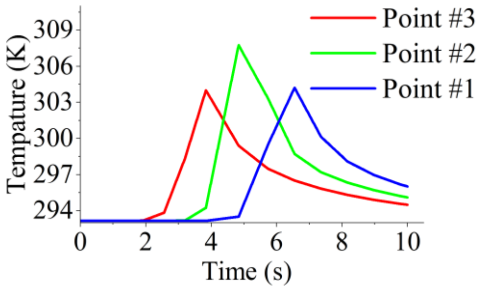

Fig.4 Temperature changes at Point#1, Point #2 and Point #3

It has been observed that the temperature changes at the three points exhibit a similarity, alternating the following process over time: the temperature rises rapidly as the heat flux approaches, achieves its peak when the center of heat flux is aligned with the point, and subsequently decreases as the heat flux moves away. The alteration at Point #1 is essentially analogous to that at point #3. However, the temperature rise at point #2 is more pronounced due to the presence of defects.

These results validate the feasibility of using active laser scanning infrared thermography technology to detect metal crack defects and provide a theoretical basis for quasi-static reconstruction methods mentioned in Section 2B.

B. Quasi-Static Reconstruction Method

The fundamental principle of the quasi-static reconstruction method is that when relative motion occurs between the heat source and the specimen, a temperature change process is induced. This process exhibits a rapid rise as the heat source approaches a specific position, reach a peek at that position, and gradually decline as the heat source moves away. This phenomenon can be conceptually understood as if each surface point were subjected to a transient point heat pulse. Furthermore, the thermal wave signals corresponding to this temperature change process at different spatial positions exhibit time-domain delays. Therefore, by compensating for these temporal delays along the direction of heat source movement, the spatial variation of the thermal wave signals under a moving heat source can be transformed into the temporal variation under a static surface pulse heat source.

As shown in Fig.5, the infrared scanning thermography process can be categorized into two distinct methods. One such method involves maintaining the infrared thermal imager and the heat source in a relatively static position. This ensures that the position of the heat source remains fixed within the imaging field of view of the infrared thermal imager, while the detection range of the specimen in the field of view changes in real time, as is shown in Fig.5(a). A further approach involves maintaining the infrared thermal imager and the specimen in a relatively static position. This ensures that the specimen remains fixed within the imaging field of view of the infrared thermal imager, while the heat source moves within the field of view, as is shown in Fig.5(b).

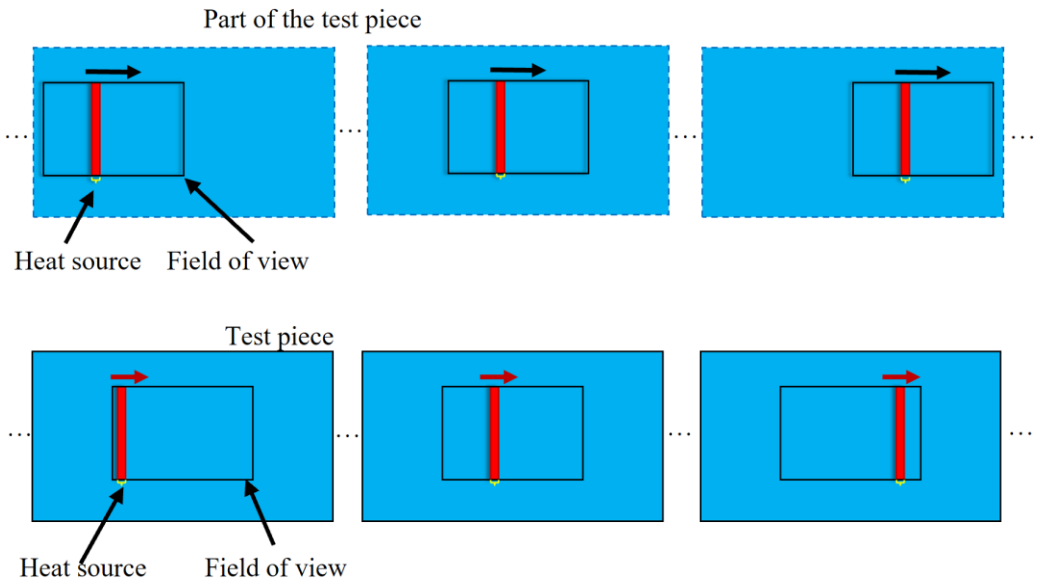

Fig.5 Two different methods of infrared scanning detection process, which (a)heat source remains fixed within the field of view and (b)heat source moves within the field of view.

A set of *ΔPixel_x* columns of pixels in the field of view, which is perpendicular to the direction of motion of the heat source, are defined as the number of column pixels to be captured for quasi-static reconstruction. The location of the *ΔPixel_x* columns of pixels in each frame captured by infrared thermal imager should be fixed in a certain area where the heat source is affecting in the current frame. Therefore, during the scanning process, *ΔPixel_x* column pixels are captured and recorded at a certain frequency as the heat source sweeps across the surface of the specimen. For the *ΔPixel_x* columns of pixels, in order to record thermal wave signals across the entire swept area, the following equation must be satisfied:

$$\Delta Pixel\_x = \frac{v}{Single\_Pixel \cdot f} \tag{1.8}$$

where $\Delta Pixel\_x$ denotes the number of column pixels to be captured, $Single\_Pixel$ indicates the physical size corresponding to a single pixel, v and f represent the scanning speed and the acquisition frequency, respectively.

The quasi-static reconstruction necessitates that the number of column pixels to be captured, designated as $\Delta Pixel\_x$, be an integer. Furthermore, the acquisition frequency, denoted by f, is constrained by the frequency of the infrared thermal imager. Consequently, it is imperative to adjust the scanning speed and the dimensions of the infrared thermal imager's field of view. This adjustment guarantees that the scanning speed, denoted by v, and the physical size corresponding to a single pixel, represented by $Single\_Pixel$, satisfy the established relationship Equation(1.8).

According to the theory, when the Equation(1.8) is satisfied, define i as the column index in each frame after reconstruction(i=1,2,⋯n).Define j as the frame index after reconstruction(j=1,2,⋯,m). As shown in Fig.6, the heat source remains fixed within the field of view, so the column index of $\Delta Pixel\_x$ columns of pixels remains unchanged in each current frame. This column index is defined as x_0. Therefore, in the (i+j-1)th raw frame, the column index corresponding to the position of the $\Delta Pixel\_x$ columns of pixels in the (i-1)th raw frame is x_0-(j-1)$\Delta Pixel\_x$. The reconstruction expression for this scanning method is obtained using formula(1.9). As shown in Fig.7, the heat source moves within the field of view. According to the Equation(1.8), the column index of $\Delta Pixel\_x$ columns of pixels changes $\Delta Pixel\_x$ in each frame. This column number is defined as x_k(k=1, 2, 3, …). Therefore, in the (i+j-1)th raw frame, the column index of column pixels corresponding to the position of the $\Delta Pixel\_x$ columns of pixels in the (i-1)th raw frame is x_{i+j-1}-(j-1)$\Delta Pixel\_x$. The reconstruction expression for this scanning method is obtained as formula(1.10).

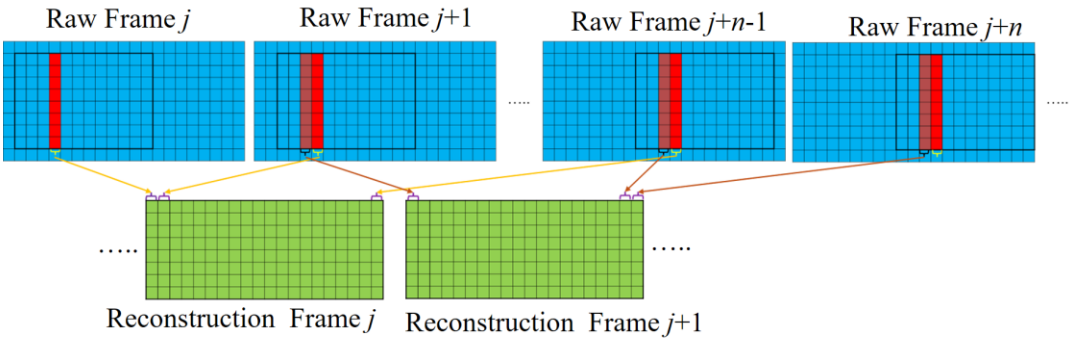

Fig.6 Reconstruction method of the scanning method shown in Fig.5(a).

$$
\begin{cases}
T_j(x_0-(j-1)\Delta Pixel\_x : x_0-(j-2)\Delta Pixel\_x-1, y) \\
\rightarrow T_j^{'}(1:\Delta Pixel\_x, y) \\
T_{j+1}(x_0-(j-1)\Delta Pixel\_x : x_0-(j-2)\Delta Pixel\_x-1, y) \\
\rightarrow T_j^{'}(\Delta Pixel\_x+1:2\Delta Pixel\_x, y) \\
\dots \\
T_{j+i-1}(x_0-(j-1)\Delta Pixel\_x : x_0-(j-2)\Delta Pixel\_x-1, y) \\
\rightarrow T_j^{'}((i-1)\Delta Pixel\_x+1:i\Delta Pixel\_x, y) \\
\dots \\
T_{j+n-1}(x_0-(j-1)\Delta Pixel\_x : x_0-(j-2)\Delta Pixel\_x-1, y) \\
\rightarrow T_j^{'}((n-1)\Delta Pixel\_x+1:n\Delta Pixel\_x, y)
\end{cases} \tag{1.9}
$$

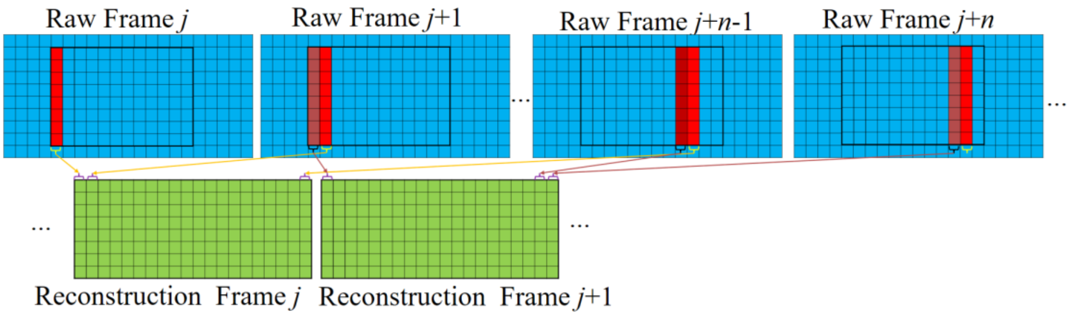

Fig.7 Reconstruction method of the scanning method shown in Fig.5(b).

$$
\begin{cases}
S_j(x_j-(j-1)\Delta Pixel\_x : x_j-(j-2)\Delta Pixel\_x-1, y) \\
\rightarrow S_j^{'}(1:\Delta Pixel\_x, y) \\
S_{j+1}(x_{j+1}-(j-1)\Delta Pixel\_x : x_{j+1}-(j-2)\Delta Pixel\_x-1, y) \\
\rightarrow S_j^{'}(\Delta Pixel\_x+1:2\Delta Pixel\_x, y) \\
\dots \\
S_{j+i-1}(x_{j+i-1}-(j-1)\Delta Pixel\_x : x_{j+i-1}-(j-2)\Delta Pixel\_x-1, y) \\
\rightarrow S_j^{'}((i-1)\Delta Pixel\_x+1:i\Delta Pixel\_x, y) \\
\dots \\
S_{j+n-1}(x_{j+n-1}-(j-1)\Delta Pixel\_x : x_{j+n-1}-(j-2)\Delta Pixel\_x-1, y) \\
\rightarrow S_j^{'}((n-1)\Delta Pixel\_x+1:n\Delta Pixel\_x, y)
\end{cases} \tag{1.10}
$$

where $T(x,y)$ and $T^{'}(x,y)$ represent the raw frame set obtained by the first scanning method and the corresponding frame set after reconstruction, respectively. $S(x,y)$ and $S^{'}(x,y)$ donates the raw frame set obtained by the second scanning method and the corresponding frame set after reconstruction, respectively.

In the frames after reconstruction, the number of row pixels remains unchanged, and the number of column pixels is $n\Delta Pixel\_x$. The image signals of the first frame after reconstruction can be considered equivalent to the thermal wave signals which are captured at the initial time when a pulsed thermal source acts on the object's surface. The image signals of the second frame after reconstruction can be regarded as the thermal wave signals which are captured Δt time after the action of the surface pulsed heat source, where $\Delta t=1/f$, and f is the acquisition frequency of the infrared camera.

To sum up, using this reconstruction method, the time-domain variation of temperature on the object's surface can be obtained, which is equivalent to the heating and cooling process after a surface pulse heat source is applied to the surface of the detected object. And different reconstruction parameters govern key output characteristics: the number of column pixels, the total frame count, and the thermal evolution within the frames after reconstruction. Under this condition, the time interval of the reconstructed frame sequence is equal to that of the captured infrared raw sequence. That is to say, the sampling frequency remains unchanged in the reconstructed virtual period.

3. MATERIALS AND METHODS

A. Specimen

In this study, a TC4 titanium alloy specimen with surface cracks are selected as the test piece, which is labeled as Specimen #01. The surfaces of the specimens are mirror polished to meet the required roughness of the surface, and the cracks on the surface are prepared by femtosecond laser etching. Five different cracks with widths ranging from 20μm to 100μm are prepared on the front surface of the specimen to determine optimal testing parameters. One crack with a width of 2μm is prepared on the back surface to validate detection capability of the method and system. The width of each crack and its corresponding identifier are specified in Tab.1.

The distributions of crack location and the optical images of the front and back of the specimen are shown in Fig.8(a) and Fig.8(b), respectively. The local micrographs of the cracks are depicted from Fig.8(c) to Fig.8(h), respectively.

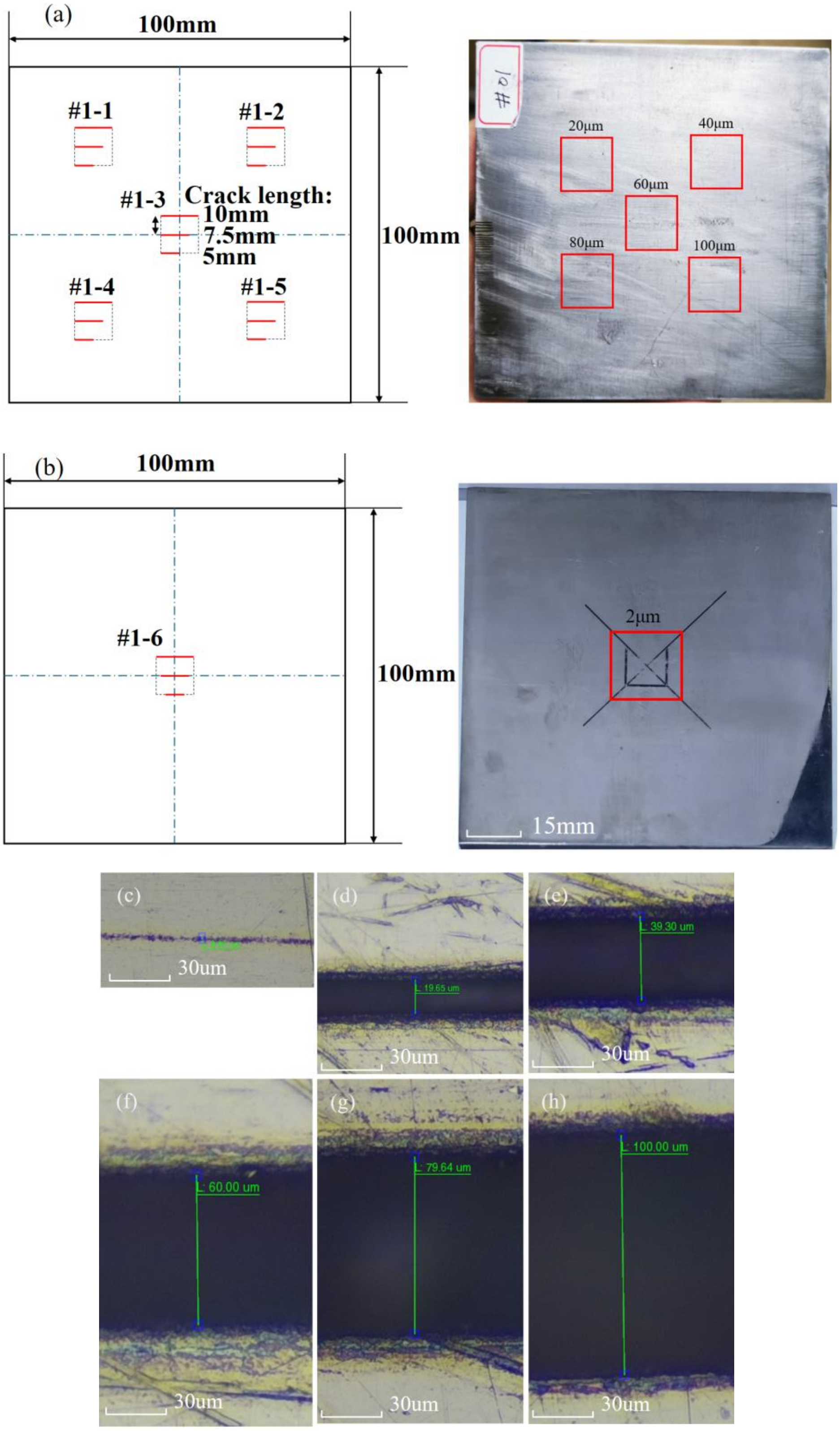

Fig.8 The distributions of crack location and the optical images of (a)the front of the specimen and (b) the back of the specimen. And the local micrographs of (c)Crack #1-6, (d)Crack #1-1, (e)Crack #1-2, (f)Crack #1-3, (g)Crack #1-4, and (h)Crack #1-5.

Tab.1 Width of simulated cracks on Specimen #1

Crack identifier	#1-1	#1-2	#1-3	#1-4	#1-5	#1-6

Crack width(μm)	20	40	60	80	100	2

B. Experimental Setup

Based on the principle of active scanning infrared imaging detection, the metal specimen crack detection system is built. The physical and schematic diagram of the system are shown in Fig.9. The entire system consists of a linear motion module with its controller, an infrared thermal imager, a collimator with a Powell lens, a laser, and a computer. The laser provides stable power in the 808nm wavelength band, which is transmitted through optical fibers. The laser is output in a linear distribution through the collimator with Powell lens and is applied the surface of the specimen. The linear motion module is connected and controlled by the computer through its controller, which allows the specimen to pass through the field of view of the infrared thermal imager at a fixed speed. The infrared image is captured by an infrared thermal imager and transmitted back to a computer for processing.

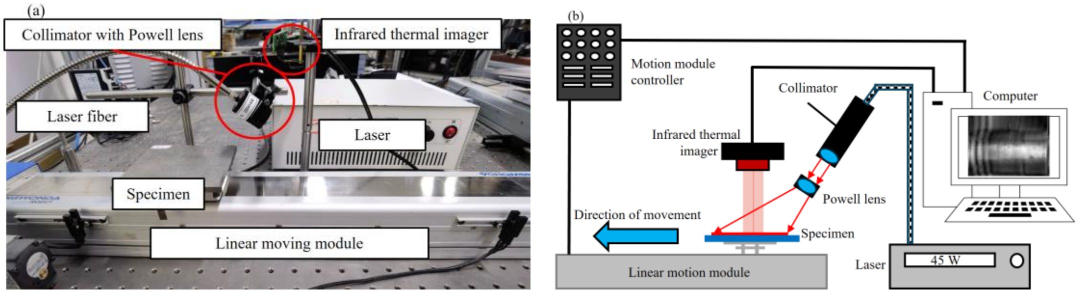

Fig.9 The (a)physical and (b)schematic diagram of the metal crack detection system.

4. EXPERIMENTAL RESULTS AND DISCUSSION

A. Comparison of results of two scanning methods

As mentioned earlier, different scanning methods correspond to different reconstruction methods. According to Equation(1.8), the scanning speed of 8.5 mm/s is obtained through pre-calibration and calculation. The detection process is facilitated by a linear laser, with the remaining test parameters delineated in Tab.2.

Tab.2 Test parameters

Laser power	Spot length	Spot width	Frame rate	*ΔPixel_x*	Scanning speed
35W	25mm	6mm	25Hz	1	8.5mm/s

Depending on the scanning method used, the numbers of column pixels in frames after reconstruction are 256 or 350, respectively. To compare and analyze the effects of these two approaches and determine the optimal reconstruction parameters, the Crack

#1-1 and Crack #1-2 are selected and tested. Two scanning methods are employed in the experiments and reconstruction, and the results are presented in Fig.10.

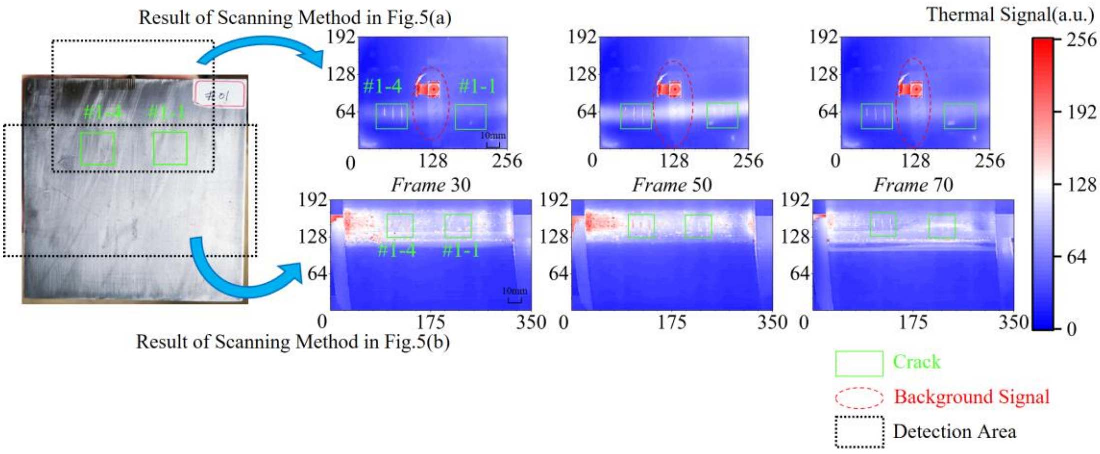

Fig.10 Reconstruction results of two scanning methods shown in (a) Fig.5(a) and (b) Fig.5(b)

It can be seen that both methods can detect Crack #1-1 and Crack #1-4 successfully. The reconstruction results of the first method shown in Fig.5(a) indicate that the entire specimen is detected, which means this method enables large-area detection with minimal interference from background signals. But the reconstruction parameters of this method are difficult to adjust, and the detection time is relatively long. The edge of the specimen in the reconstruction results appear curved, which is caused by the combined interference of reconstruction parameters and lens distortion from the infrared thermal imager. This issue can be resolved by adjusting the camera lens. The detection results of the second method shown in Fig.5(b) demonstrate that the cracks and their surrounding areas are detected, which means this method is suitable for small-area detection because the detection area is limited by the camera field of view. A relatively short time is taken by this method, and simple reconstruction parameters are required. The shortcoming is, the results of the second method contain obvious background signals, which are circled with dotted lines. These thermal signals are captured because the thermal signals from the infrared thermal imager itself are reflected off metal surfaces, which cannot be eliminated solely through reconstruction.

To reduce the influence of background signals, the following experiments all adopt the first scanning method. As mentioned in Section 2B, the content of the frames after reconstruction, shaped by the chosen reconstruction parameters, is a direct determinant of detection performance. To determine the optimal reconstruction parameters, multiple experiments are conducted using Crack #1-1, Crack #1-2, Crack #1-3, Crack #1-4 and Crack #1-5, yielding the optimal results among frames after reconstruction as shown in Fig.11.

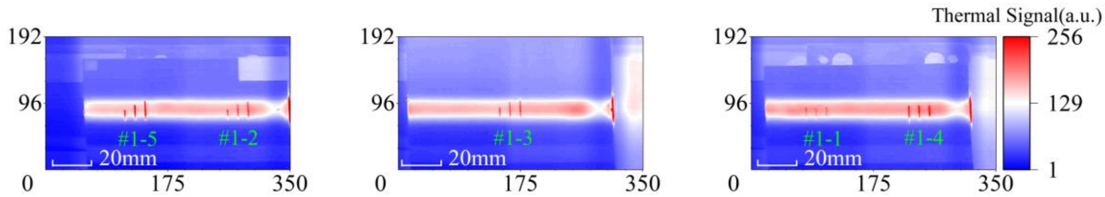

Fig.11 Reconstruction results of cracks on the front of Specimen #01.

B. Analysis of results of Crack #1-6 with a width of 2μm

Based on the adjusted field of view of the infrared thermal imager, the distance between the infrared thermal imager and the specimen is set as 15cm. According to Equation(1.8), the scanning speed of 0.85 mm/s is obtained through pre-calibration and calculation. Considering the optimal reconstruction parameters, the number of column pixels in frames after reconstruction is 2400. The remaining test parameters are shown in Tab.3.

Tab.3 Test parameters

Laser power	Spot length	Spot width	Frame rate	$\Delta Pixel\_x$	Scanning speed
35W	10mm	6mm	15Hz	1	0.85mm/s

The detection of Crack #1-6 is accomplished and the ideal frame from the results after reconstruction is shown in Fig.12(a), Fig.12(b) and Fig.12(c). The thermal signals corresponding to the pixel in the 185th row are obtained and shown in Fig.12(d).

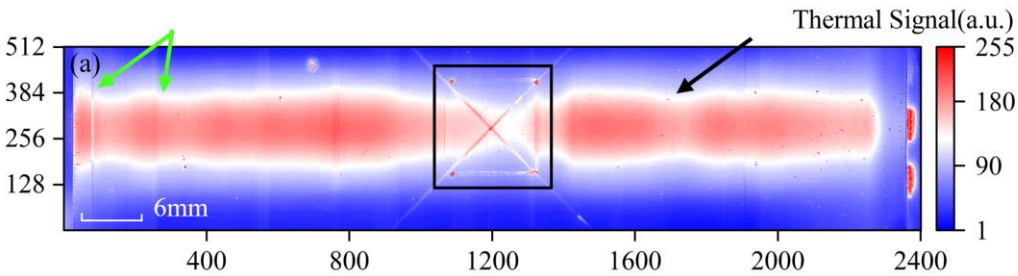

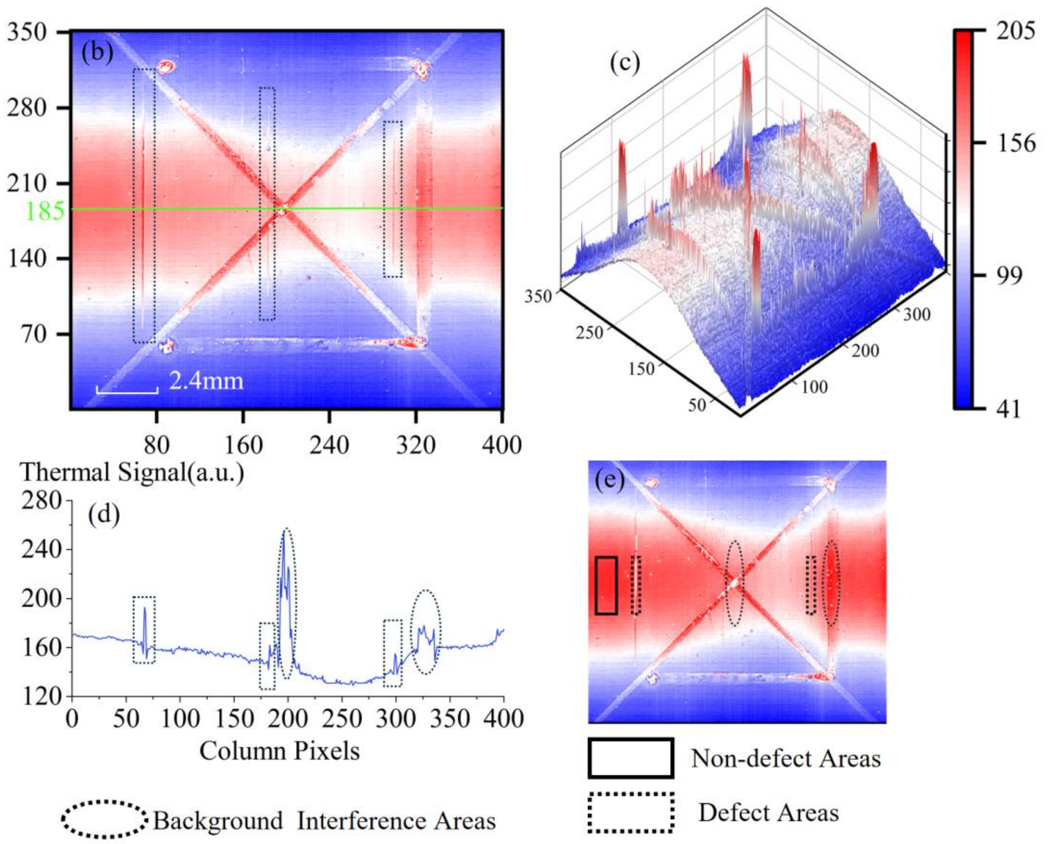

Fig.12 Reconstruction results of Crack#1-6, which display (a)the overall result, (b,c)the local result around Crack #1-6 ,(d)the thermal signals corresponding to the pixel in the 185th row and (e)the selection of defect and non-defect areas in Crack #1-6, respectively.

It can be seen that three defects of Crack #1-6 can be detected, and the thermal signals at the defect site are higher than those of the surrounding defect-free area, which is consistent with the theoretical simulation results in Section 2A. The laser-irradiated area on the specimen exhibits distinctly elevated thermal signals, which remain relatively stable but show fluctuations in the width of the area. This phenomenon under discussion can be attributed to two primary factors. Firstly, it is evident that the unstable frame capture rate of infrared thermal imagers results in varying actual time intervals between frames, leading to changes in the diffusion effect of captured thermal signals on the specimen. This variation is characterized by its relative uniformity, as illustrated by the black arrows in Fig.12(a). Secondly, the infrared thermal imager's inherent shutter correction capability can result in duplication or gaps in the acquired source image sequence. This variation is more pronounced, as indicated by the green arrows in Fig.12(a). More importantly, as the number of frames involved in reconstruction increases, this effect gradually becomes more pronounced.

To quantitatively analyze the detection results, the signal-to-noise ratio (SNR) formula is defined as follows:

$$SNR = \frac{|P_D - P_N|}{\sigma_N} \tag{1.11}$$

where P_D and P_N represent the mean of characteristic values representing defect and non-defect areas, respectively. σ_N donates the standard deviation of characteristic values representing non-defect areas. The selection of defect and non-defect areas in Crack #1-6 is shown in Fig.12(e), which non-defect areas are outlined with solid lines and defect areas are indicated with dotted lines. Based on Fig.12(b) and Fig.12(d), after excluding temperature abrupt variations caused by background interference, the pixels in columns 67-69 and 299-301 are selected as the most ideal defect areas. The non-defect area is selected in the area that is also heated, has no surface defects and exhibits the smallest adjacent temperature change, such as the pixels in columns 15-35.

A similar region selection is performed for Crack #1-1, Crack #1-2, Crack #1-3, Crack #1-4 and Crack #1-5, and the SNR is calculated respectively. The resulting SNR values for all cracks are summarized in Tab.4. It is observed that wider cracks tend to exhibit higher SNR, while narrower cracks(e.g., Crack #1-1 and Crack #1-6) demonstrate lower SNR, leading to a challenge of discernment.

Tab.4 The SNR of the cracks

Crack identifier	#1-1	#1-2	#1-3	#1-4	#1-5	#1-6
SNR	34.4376	37.7160	40.2322	45.6894	54.9652	20.0632

C. Comparison of Feature Extraction Results

The above results demonstrate that through the results after reconstruction, detection and discrimination of cracks with larger widths can be achieved more easily than that of cracks with smaller widths, such as Crack #1-1 and Crack #1-6. Meanwhile, the results after reconstruction are equivalent to those under a static pulse surface heat source, allowing for analysis using established feature extraction techniques. Therefore, to improve the reliability of crack detection results, it’s necessary to use feature extraction algorithm to process the reconstructed results, with subsequent identification performed on the processed feature image.

The results after feature extraction are obtained using Fourier Transformation (FT), Principal Component Transformation (PCT), and Partial Least Squares Transformation (PLST), respectively. The SNR of cracks processed with different feature extraction algorithms are calculated and the results are shown in Fig.15. To ensure consistent imaging standards across different algorithms, the data normalization is performed, yielding the results of Crack #1-1 and Crack #1-6 are shown in Fig.13 and Fig.14.

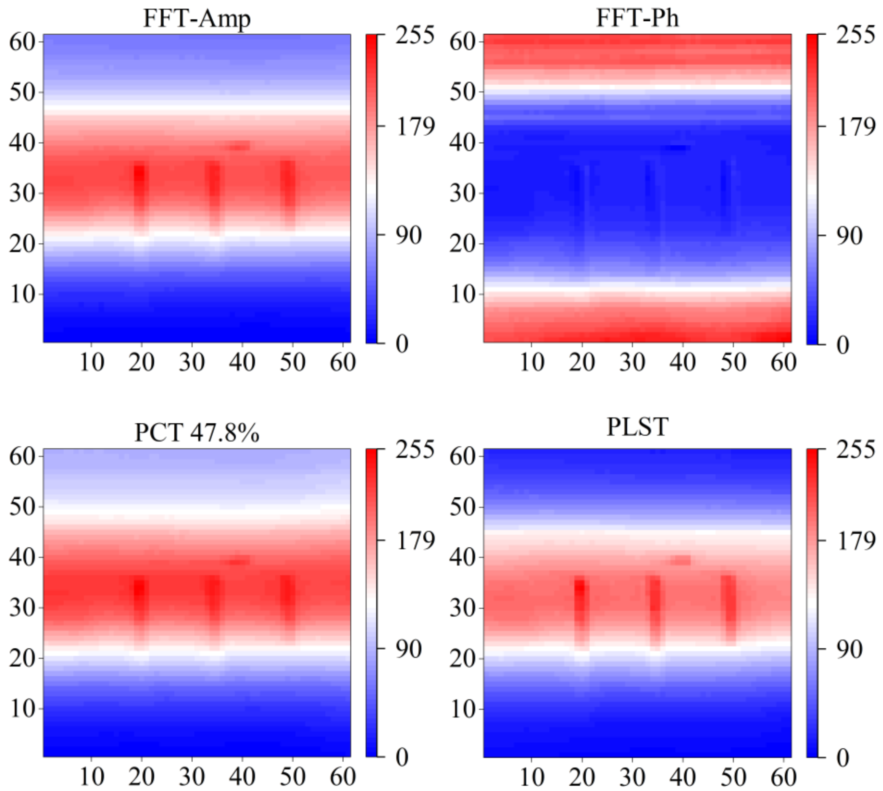

Fig.13 Results of Crack #1-1 after feature extraction, based on (a)amplitude characteristics obtained from FT, (b)phase characteristics obtained from FT, (c)the first principal component obtained from PCT which accounts for 47.8%, and (d) characteristics obtained from PLST.

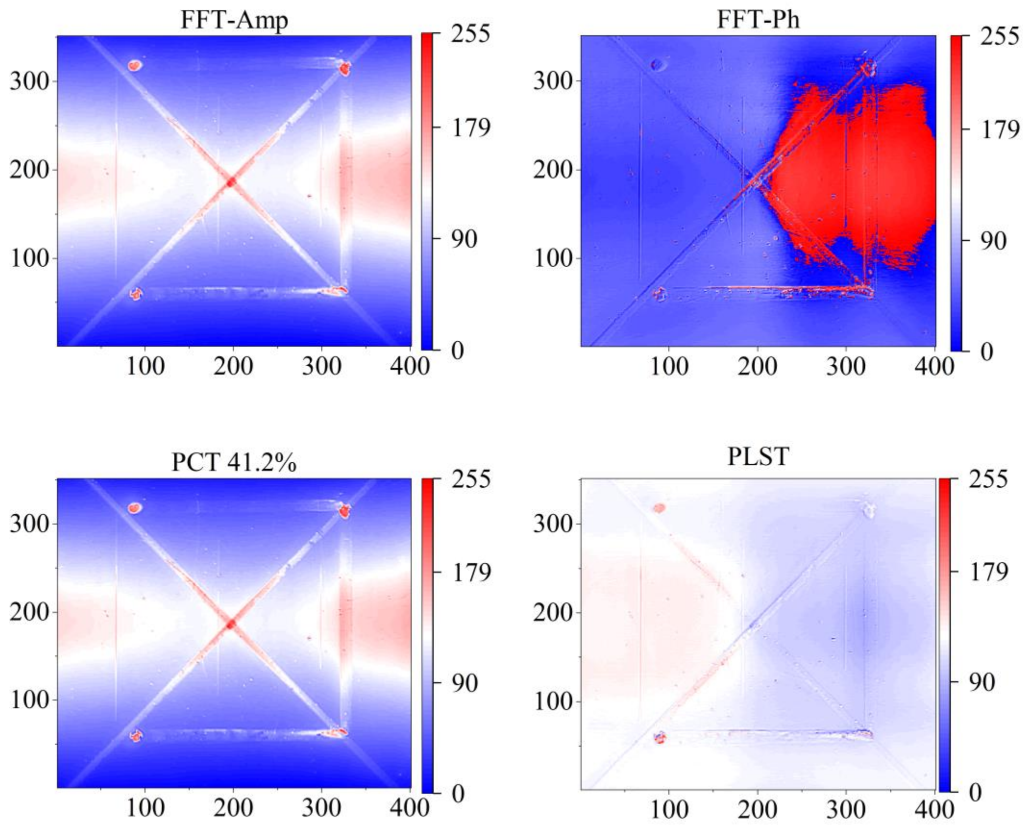

Fig.14 Results of Crack #1-6 after feature extraction, based on (a)amplitude characteristics obtained from FT, (b)phase characteristics obtained from FT, (c)the first principal component obtained from PCT which accounts for 41.2%, and (d) characteristics obtained from PLST.

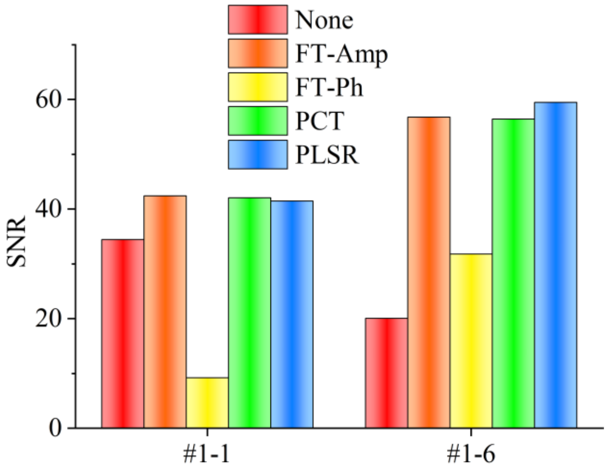

Fig.15 The SNR of Crack #1-1 and Crack #1-6 using different feature extractions algorithms.

It can be found that all algorithms except for FT-Ph provide a contribution to the improvement of SNR of Crack #1-1. While for Crack #1-6, all the algorithms provide a more substantial SNR enhancement. This indicates that feature extraction algorithms can effectively improve the SNR of cracks, thereby facilitating the identification and detection. Furthermore, the improvement is more pronounced for cracks with lower SNR.

5. Conclusions

This paper proposes a laser scanning infrared thermography based on thermal signal spatial quasi-static reconstruction for the purpose of detecting microcracks on the surface of metal materials. The method is supported by theoretical analysis and experimental validation. Through the established three-dimensional thermal wave diffusion model under a moving linear heat source, the simulation results demonstrate that the model effectively distinguishes the temperature differences between the area with and without defects. Furthermore, the temperature variations at different positions along the scanning direction of the extended heat source exhibit a similarity in the frequency domain and a delay in the time domain. Based on basic principles and differences in scanning methods, the quasi-static reconstruction method and the reconstruction formulas corresponding to different situations are proposed. Subsequently, an experimental system is built to inspect microcracks on metal specimens. Cracks with widths ranging from 2 μm to 100 μm are then prepared and tested.

The experimental results confirm that the quasi-static reconstruction method is adaptable to various detection configurations and can reliably detect cracks as narrow as 2 μm. For cracks that are not clearly discernible from results before or after reconstruction, the application of feature extraction algorithms helps to enhance crack features with a minimum width of 2μm, leading to the improvement of crack SNR.

In conclusion, the results confirmed the practicality and versatility of the quasi-static reconstruction method, particularly in reliably detecting 2μm cracks, which highlights its adaptability in detecting microcracks on the highly reflective surface of metal. Additionally, the detection system is easily miniaturized and integrated, facilitating its application with various infrared thermal imagers and scanning types, positioning it as a promising tool for in-situ and endoscopic inspections in critical industries such as aerospace, power generation, and precision manufacturing. Future applications could extend beyond flat titanium alloys to include curved components, internal surfaces of pipes or turbines, and other high-value metallic or even ceramic materials under real operational environments. Future advancements will focus on enhancing system robustness and intelligence. This includes the development of software to compensate and suppress effects arising from camera instability and thermal diffusion, enabling faster, adaptive scanning via automated processing, and integrating AI for objective crack detection. The combination of this method with other non-destructive testing techniques will facilitate comprehensive defect characterization in complex materials and structures.

References

[1] Madhulika Srivastava, et al. "Additive manufacturing of Titanium alloy for aerospace applications: Insights into the process, microstructure, and mechanical properties." Applied Materials Today 41.(2024):102481-102481.doi:10.1016/J.APMT.2024.102481.

[2] Mikael Perrut, et al. "High temperature materials for aerospace applications: Ni-based superalloys and γ -TiAl alloys."Comptes rendus - Physique 19.8(2018):657-671.doi:10.1016/j.crhy.2018.10.002.

[3] Athanasios Iliopoulos, et al. "Crack Growth in a Range of Additively Manufactured Aerospace Structural Materials." Aerospace 5.4(2018):doi:10.3390/aerospace5040118.

[4] A.K. Syed, X. Zhang, and M.E. Fitzpatrick. "A comparison of fatigue crack growth performance of two aerospace grade aluminium alloys reinforced with

bonded crack retarders." Fatigue & Fracture of Engineering Materials & Structures 41.5(2018):1237-1242.doi:10.1111/ffe.12744.

[5] Xuesong Zhang,Yongjun Chen,and Junling Hu. "Recent advances in the development of aerospace materials." Progress in Aerospace Sciences 97.(2018):22-34.doi:10.1016/j.paerosci.2018.01.001.

[6] Strohmann Tobias, et al. "Next generation fatigue crack growth experiments of aerospace materials." Scientific Reports 14.1(2024):14075-14075.doi:10.1038/S41598-024-63915-X.

[7] Liu Zhiying, et al. "Fatigue crack growth behavior of an additively manufactured titanium alloy: Effects of spatial and crystallographic orientations of α lamellae." International Journal of Plasticity 172.(2024):103819-.doi:10.1016/J.IJPLAS.2023.103819.

[8] Rafał Radecki, et al. "Nonlinear Crack-Wave Modulations in Shear Horizontal Wave Propagation for Fatigue Crack Detection." Journal of Sound and Vibration 595. (2025):118758-118758.doi:10.1016/J.JSV.2024.118758.

[9] Rong Wang, et al. "Nonlinear ultrasonic detection for evaluating fatigue crack in metal plate." Structural Health Monitoring 18.3(2019):869-881.doi:10.1177/1475921718784451.

[10] Tubei Valary, et al. "Direct observation of three-dimensional short fatigue crack closure behavior in Ti-6Al-4V alloy using ultra-high-resolution X-ray microtomography." International Journal of Fatigue 168.(2023):doi:10.1016/J.IJFATIGUE.2022.107428.

[11] Dong Lihong, et al. "Monitoring fatigue crack propagation of ferromagnetic materials with spontaneous abnormal magnetic signals." International Journal of Fatigue 30.9(2007):1599-1605.doi:10.1016/j.ijfatigue.2007.11.009.

[12] P C Meijers, D H Malschaert, and M Veljkovic. "Monitoring fatigue crack growth using magnetic stray field measurements." Journal of Physics: Conference Series 2647.18(2024):doi:10.1088/1742-6596/2647/18/182018.

[13] N.J. Shipway, et al. "Automated defect detection for Fluorescent Penetrant Inspection using Random Forest." NDT and E International 101.(2019):113-123.doi:10.1016/j.ndteint.2018.10.008.

[14] Niccolai Alessandro, et al. "Machine Learning-Based Detection Technique for NDT in Industrial Manufacturing." Mathematics 9.11(2021):1251-1251.doi:10.3390/MATH9111251.

[15] Liang Cheng,and Gui Yun Tian. "Surface Crack Detection for Carbon Fiber Reinforced Plastic (CFRP) Materials Using Pulsed Eddy Current Thermography." IEEE sensors journal 11.12(2011):3261-3268.

[16] L. D. Favro, et al. "Infrared imaging of defects heated by a sonic pulse." Review of Scientific Instruments 71.6(2000):2418-2421.doi:10.1063/1.1150630.

[17] Changhang Xu, et al. "An infrared thermal image processing framework based on superpixel algorithm to detect cracks on metal surface." Infrared Physics and Technology 67.(2014):266-272.doi:10.1016/j.infrared.2014.08.002.

[18] Cui Shuanglong, et al. "Research on Crack Detection Method of Ballastless Track Slab Based on Infrared Thermometer." Infrared Physics & Technology prepublish(2021):103772-.doi:10.1016/J.INFRARED.2021.103772.

[19] Chengji Mi, et al. "Quantitative thermographic estimation of fatigue crack propagation behavior for TC4 titanium alloy based on deep learning algorithm." Theoretical and Applied Fracture Mechanics 140.(2025):105166-105166.doi:10.1016/J.TAFMEC.2025.105166.

[20] Qi Fang Zhu, et al. "Thermal Non-Destructive Testing for the Titanium Implants." Advanced Materials Research 2605.785-786(2013):52-57.doi:10.4028/www.scientific.net/AMR.785-786.52.

[21] Balaji Ragupathi, et al. "Online monitoring of pre-crack initiation in carbon fiber-reinforced thermoplastic composites by an ultrasonic cutting tool using high-speed optical imaging and infrared thermography." Ultrasonics 143.(2024):107411-107411.doi:10.1016/J.ULTRAS.2024.107411.

[22] Fei Wang, et al. "Enhanced recognition of the solid propellant grain internal surface closed cracks detection by robot-assisted rotary linear laser scanning thermography." Measurement 248.(2025):116774-116774.doi:10.1016/J.MEASUREMENT.2025.116774.

[23] Wang Fei, et al. "Multimode infrared thermal-wave imaging in non-destructive testing and evaluation (NDT&E): Physical principles, modulated waveform, and excitation heat source." Infrared Physics and Technology 135.(2023):doi:10.1016/J.INFRARED.2023.104993.